

# L1506 : a prestellar core in the making <sup>★</sup>

L. Pagani<sup>1</sup>, I. Ristorcelli<sup>2</sup>, N. Boudet<sup>2</sup>, M. Giard<sup>2</sup>, A. Abergel<sup>3</sup>, and J.-P. Bernard<sup>2</sup>

<sup>1</sup> LERMA & UMR 8112 du CNRS, Observatoire de Paris, 61 Av. de l'Observatoire, 75014 Paris, France

e-mail: laurent.pagani@obspm.fr

<sup>2</sup> CESR & UMR 5187 du CNRS/Université de Toulouse, 9 Av. du Colonel Roche, BP 4346, 31028 Toulouse Cedex 4, France

e-mail: ristorcelli@cesr.fr, giard@cesr.fr, bernard@cesr.fr

<sup>3</sup> IAS, Bât. 121, Université Paris-Sud F-91435 Orsay

e-mail: alain.abergel@ias.u-psud.fr

Received 09/07/2009; accepted 02/12/2009

## ABSTRACT

**Context.** Exploring the structure and dynamics of cold starless clouds is necessary to understand the different steps leading to the formation of protostars. Because clouds evolve slowly, many of them must be studied *in detail* to pick up different moments of a cloud's lifetime.

**Aims.** We study here a fragment of the long filament L1506 in the Taurus region which we name L1506C, a core with interesting dust properties which have been evidenced with the PRONAOS balloon-borne telescope.

**Methods.** To trace the mass content of L1506C and its kinematics, we mapped the dust emission, and the line emission of two key species, C<sup>18</sup>O and N<sub>2</sub>H<sup>+</sup>. <sup>13</sup>CO and C<sup>17</sup>O were also observed. We model the species emission using 1D Monte Carlo models.

**Results.** This cloud is reminiscent of L1498 but also shows peculiar features: i) a large envelope traced solely by <sup>13</sup>CO holding a much smaller core with a strong C<sup>18</sup>O depletion in its center despite a low maximum opacity ( $A_V \sim 20$  mag), ii) extremely narrow C<sup>18</sup>O lines indicating a low, non-measurable turbulence, iii) contraction traced by C<sup>18</sup>O itself (plus rotation), iv) unexpectedly, the kinematical signature from the external envelope is opposite to the core one: the <sup>13</sup>CO and C<sup>18</sup>O velocity gradients have opposite directions and the C<sup>18</sup>O line profile is blue peaked on the contrary to the <sup>13</sup>CO one which is red peaked. The core is large ( $r = 3 \times 10^4$  A.U.) and not very dense ( $n(\text{H}_2) \leq 5 \times 10^4 \text{ cm}^{-3}$ , possibly less). This core is therefore not prestellar yet.

**Conclusions.** All these facts suggest that the core is kinematically detached from its envelope and in the process of forming a prestellar core. This is the first time that the dynamical formation of a prestellar core is witnessed. The extremely low turbulence could be the reason for the strong depletion of this core despite its relatively low density and opacity in contrast with undepleted cores such as L1521E which shows a turbulence at least 4 times as high.

**Key words.** Stars: formation – ISM: clouds – ISM: abundances – ISM: molecules – ISM: Structure – ISM: individual: L1506

## 1. Introduction

On their way to form stars, clouds go through a contraction phase leading to the formation of prestellar cores ( $n \geq 1 \times 10^5 \text{ cm}^{-3}$ , Keto & Caselli 2008) which are usually identified by their lack of internal heating sources, their large CO depletion, and their strong NH<sub>3</sub> and N<sub>2</sub>H<sup>+</sup> emission lines for which turbulence is often subthermal. These cores subsequently collapse to form protostars. Many details pertaining to these two condensation steps are still obscure and we don't understand what conditions are necessary to produce stars of different masses, high or low, what conditions are necessary to start the contraction of the cloud or the collapse of the prestellar core, nor the rôle of the magnetic field in supporting the clouds against collapse, etc... Obviously as the evolution time is long, one has to observe many clouds as a substitute to tracking any single cloud in the process of forming a star. For each cloud, physical and chemical properties should be studied in detail to assess all important parameters such as temperature, density, kinematics, and their respective gradients, if any, and also chemical abundances by volume. By accumulating this type of studies, we can hope to disentangle depletion phenomenon versus cloud age or density, contraction versus os-

cillation, etc. and describe how prestellar cores and protostars form.

Many prestellar cores have been identified and some have already been studied in detail, including B68, L183, L1498, L1544, etc. Among these objects a few cases have been identified as *early prestellar cores* if their density is already greater than  $1 \times 10^5 \text{ cm}^{-3}$ , or *simple cores* probably about to form prestellar cores if not. The first type includes L1495B, L1521B, and L1521E (Hirota et al. 2002, 2004; Tafalla & Santiago 2004) which, despite a high density, show no sign of depletion (strong CO lines, weak or absent NH<sub>3</sub> and N<sub>2</sub>H<sup>+</sup> lines) and are considered as being both physically and chemically young while the second type is represented by two cases presently, L1498 (Tafalla et al. 2004; Shirley et al. 2005) and the very dense globule 'G2' in the Coalsack complex (Lada et al. 2004). L1498 in the study by Shirley et al. (2005) exhibits a low density ( $1-3 \times 10^4 \text{ cm}^{-3}$ ) and molecular depletion (already reported by several other authors, especially Willacy et al. 1998, who, by studying L1498, reported the first C<sup>18</sup>O depletion in a prestellar core by comparison with a dust map). The G2 gas content has not been studied in detail yet and only its peculiar, ring-like dust shape indicates its unstable nature despite its low density. This core is expected to turn into a prestellar core (Lada et al. 2004). In this second category, which is considered as physically young but

<sup>★</sup> based on observations made with the IRAM-30m. IRAM is supported by INSU/CNRS (France), MPG (Germany), and IGN (Spain).

chemically evolved, we present a newcomer, a fraction of the L1506 filament.

The cloud we present in this paper, L1506, has attracted attention during a large-scale  $^{13}\text{CO}$  survey (Abergel et al. 1994) because of its low (though not unique) DIRBE<sup>1</sup>  $I_{140\mu\text{m}}/I_{240\mu\text{m}}$  and IRAS<sup>2</sup>  $I_{60\mu\text{m}}/I_{100\mu\text{m}}$  colour ratios to which the  $^{13}\text{CO}$  maps were compared. Its dust properties were studied later on using the PRONAOS<sup>3</sup> balloon-borne experiment continuum emission data in the submillimeter range (200 – 600  $\mu\text{m}$ ) (Stepnik et al. 2003), albeit with a limited angular resolution (2–3.5'). A significant change of the dust properties has been revealed going from the diffuse to the dense part of the cloud: no emission from transiently heated small particles, and a strong enhancement (by a factor of 3.4) of the submillimeter emissivity in the latter. This was interpreted as the signature of dust coagulation leading to the formation of fluffy aggregates (made of a mixture of very small and big grains). In order to understand this evolution and investigate what are the physical conditions associated with efficient aggregate formation (ice mantles, level of turbulence, densities, etc.), we are now concentrating on the study of the gas properties. It is presently clear that depletion plays a key rôle in the gas phase of dark clouds and basically two species are needed to map the clouds, namely  $\text{C}^{18}\text{O}$  and  $\text{N}_2\text{H}^+$ .  $\text{NH}_3$  is also a good tracer but  $\text{N}_2\text{H}^+$  has some advantages over  $\text{NH}_3$  among which the possibility to use the same telescope as for  $\text{C}^{18}\text{O}$ , giving a similar resolution and beam correction and also superior diagnostic capabilities as discussed by Pagani et al. (2007). By observing these species, both the undepleted (outer) and the depleted (inner) cores can be traced and their kinematics and physical properties can be modeled. With  $^{13}\text{CO}$ , we will also be able to trace a fraction of the extended envelope. We present and model such observations in this paper and discuss the properties of this cloud.

## 2. Observations

All observations were performed using the IRAM-30m telescope<sup>4</sup>. The dark nebula L1506 is an elongated object (Onishi et al. 1996; Nercessian et al. 1988) and the SIMBAD<sup>5</sup> reference position ( $\alpha_{2000} = 4^{\text{h}}18^{\text{m}}31.1^{\text{s}}$   $\delta_{2000} = +25^{\circ}19'25''$ ) is outside the part of the cloud we present here which is centered on the PRONAOS emission peak ( $\alpha_{2000} = 4^{\text{h}}18^{\text{m}}50^{\text{s}}$   $\delta_{2000} = +25^{\circ}19'15''$ , Stepnik et al. 2003) which we propose to name L1506C (A and B are already defined, Lee & Myers 1999). Its distance is estimated to be 140 pc (Elias 1978; Kenyon et al. 1994).

In september 2004, we mapped the filament dust emission at 1.2 mm with the MAMBO<sup>6</sup> II bolometer. Skydips, pointings and calibration source observations were regularly performed, and data reduction was executed using IRAM proprietary software. The cold filament studied by Stepnik et al. (2003) is clearly visible at the centre (Fig. 1). Spectroscopic observations were performed over several runs: 29 & 30 November 2003, 22 & 23 May 2004, 28 July 2004 and 18 July 2008. In all cases, the VESPA<sup>7</sup>

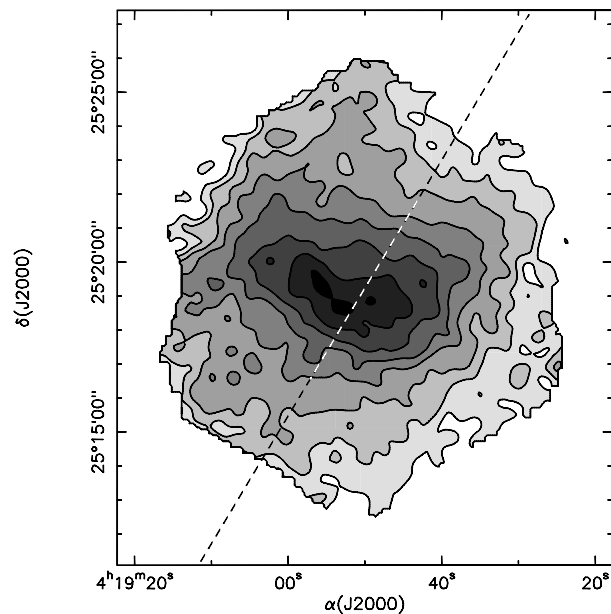


**Fig. 1.** Dust emission at 1.2 mm as measured by MAMBO II. Resolution has been degraded to 30'' for a better signal-to-noise ratio. Levels are spaced by 0.5 MJy sr<sup>-1</sup> from 0.5 to 4 MJy sr<sup>-1</sup>. The dashed line represents the cut observed with PRONAOS, and the white section the fraction of the cut observed with the IRAM-30m. The original cut direction was chosen to be perpendicular to the FIR filament (colour image on-line). The (0,0) position corresponds to  $\alpha_{2000} = 4^{\text{h}}18^{\text{m}}50^{\text{s}}$   $\delta_{2000} = +25^{\circ}19'15''$ .

autocorrelator was used with frequency sampling varying from 6 to 20 kHz for 3 mm lines and 40 kHz for 1.3 mm lines (Table 1). All observations were done in frequency switching mode. Receivers A&B were used except in July 2008 where the 1 mm 9 pixel cameras HERA<sup>8</sup> 1&2 were used in the On-the-Fly mode, still using frequency switching. The  $\text{C}^{18}\text{O}$  and  $^{13}\text{CO}$  (J:1–0) lines were observed simultaneously by tuning the receiver halfway between the two frequencies and offsetting the VESPA autocorrelator subwindows by  $\pm 210$  MHz in front of the two lines. Pointing was regularly checked and found to be stable within 3''.

**Table 1.** Telescope settings

Line	Frequency (MHz)	Beam size (")	Sampling (kHz)	Sampling (m s <sup>-1</sup> )
$\text{N}_2\text{D}^+$ (J:1–0)	77 109.616 <sup>a</sup>	32	6	23
$\text{N}_2\text{H}^+$ (J:1–0)	93 173.764 <sup>a</sup>	27	10	32
$\text{C}^{18}\text{O}$ (J:1–0)	109 782.176	23	10	27
$^{13}\text{CO}$ (J:1–0)	110 201.360	23	20	54
$\text{C}^{17}\text{O}$ (J:1–0)	112 358.982 <sup>b</sup>	23	10	27
$\text{C}^{18}\text{O}$ (J:2–1)	219 560.358	12	40	54

<sup>a</sup> New frequency for the main  $\text{J}_{\text{FF}'}:1_{23} \rightarrow 0_{12}$  hyperfine component from Pagani et al. (2009a)

<sup>b</sup>  $\text{J}_{\text{F}}:1_{7/2}-0_{5/2}$  transition from Klapper et al. (2003)

<sup>1</sup> Diffuse Infra Red Background Experiment, <http://lambda.gsfc.nasa.gov>

<sup>2</sup> Infra Red Astronomical Satellite, <http://lambda.gsfc.nasa.gov>

<sup>3</sup> PROgramme NAational d'Observations Submillimétriques

<sup>4</sup> <http://www.iram-institute.org/>

<sup>5</sup> <http://simbad.u-strasbg.fr/sim-fid.pl>

<sup>6</sup> MAx-Planck-Millimeter-BOLometer, see IRAM website

<sup>7</sup> VErsatile Spectroscopic and Polarimetric Analyzer, see IRAM website

<sup>8</sup> HEterodyne Receiver Array, see IRAM website

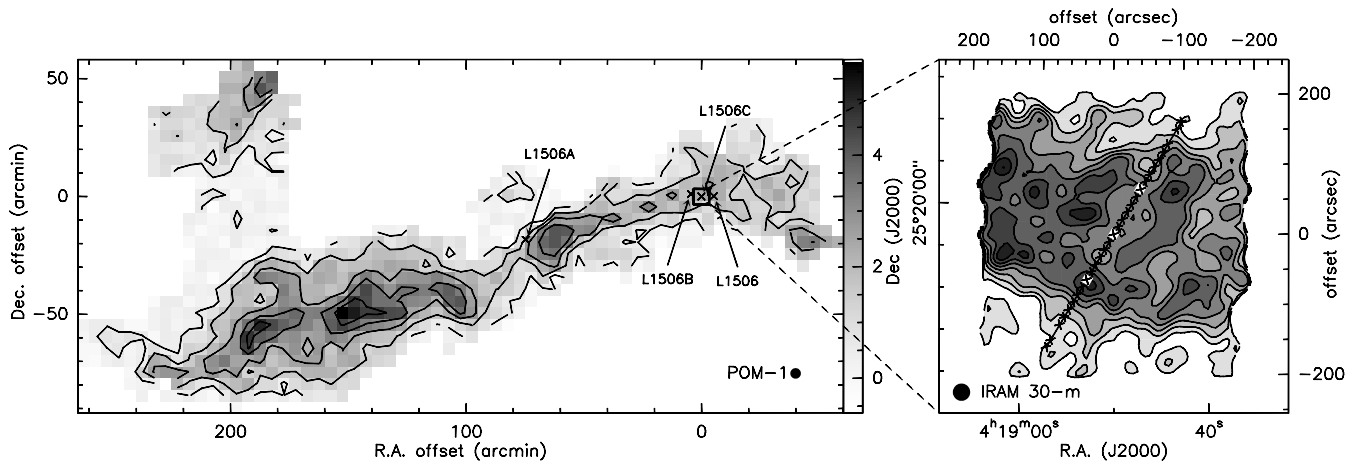


**Fig. 2.** **Left:** low resolution  $^{13}\text{CO}$  (J:1–0) integrated intensity map of the L1506 Taurus cloud filament (original data from Nercessian et al. 1988). Contour levels are 0.5 to 4.5  $\text{K km s}^{-1}$  by steps of 1  $\text{K km s}^{-1}$ . The POM-1 2.5-m dish has a 4.5' resolution as shown in the bottom right corner. The square indicates the surface mapped in  $\text{C}^{18}\text{O}$  (J:2–1). The offsets are with respect to L1506C coordinates (see text). **Right:** the smoothed  $\text{C}^{18}\text{O}$  (J:2–1) integrated intensity map. Superposed to the map is the strip path observed with PRONAOS (Stepnik et al. 2003) along which we observed  $^{13}\text{CO}$ ,  $\text{C}^{18}\text{O}$ , and  $\text{N}_2\text{H}^+$  with a good signal to noise ratio (see Fig. 3). The crosses indicate the observed points and the 3 white boxes (superposed to 3 crosses) the points observed also in  $\text{C}^{17}\text{O}$  (see Fig. 5). The degraded 30-m beam size is represented. Levels are from 0.1 to 0.7  $\text{K km s}^{-1}$  by steps of 0.1  $\text{K km s}^{-1}$ . The (0,0) position corresponds to  $\alpha_{2000} = 4^{\text{h}}18^{\text{m}}50^{\text{s}}$   $\delta_{2000} = +25^{\circ}19'15''$ .

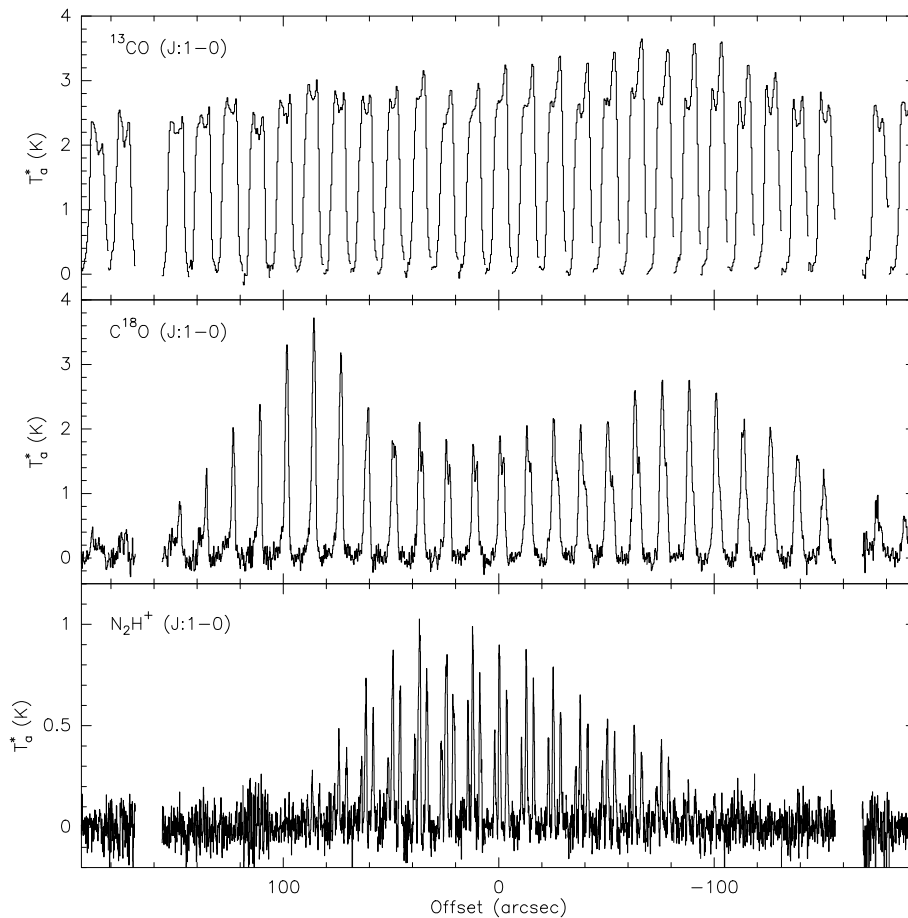


**Fig. 3.** Spectra taken along the PRONAOS cut (see Fig. 2). The upper row shows the  $^{13}\text{CO}$  (J:1–0) spectra. The middle row shows the  $\text{C}^{18}\text{O}$  (J:1–0) spectra. The lower row shows the  $\text{N}_2\text{H}^+$  (J:1–0) spectra. The velocity scale is 6.5 to 8  $\text{km s}^{-1}$  for  $^{13}\text{CO}$  and  $\text{C}^{18}\text{O}$ , and 5.5 to 9  $\text{km s}^{-1}$  for  $\text{N}_2\text{H}^+$ . Offsets increase from North-West to South-East.

### 3. Results and analysis

Figure 2 shows a large-scale  $^{13}\text{CO}$  (J:1–0) map obtained with POM-1<sup>9</sup> (a 2.5 m dish telescope with 4.5' resolution and 100

$\text{km s}^{-1}$  filters – 0.27  $\text{km s}^{-1}$  – which was in service at Bordeaux Observatory. Original data taken from Nercessian et al. 1988), and the region of interest is delineated by a square. This map traces the large-scale envelope of the cloud. On the right-hand-side, the  $\text{C}^{18}\text{O}$  (J:2–1) integrated intensity map obtained on-the-fly with the 30-m over L1506C is shown. We degraded the res-

<sup>9</sup> *Petite Opération Millimétrique*

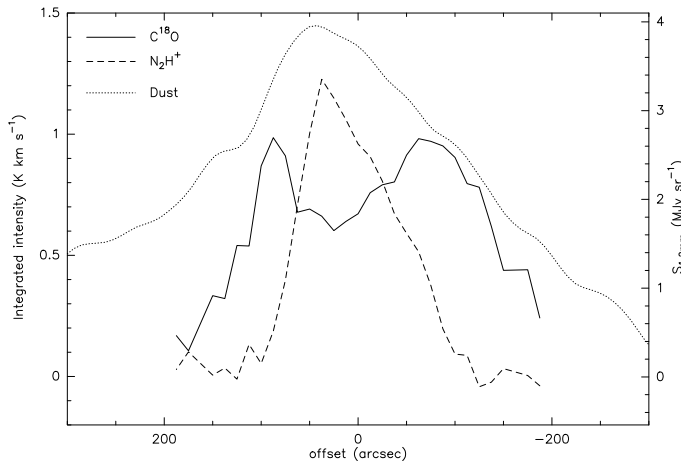


**Fig. 4.** Integrated intensity of  $C^{18}O$  and  $N_2H^+$  (J:1–0) compared to the dust emission as measured by MAMBO along the PRONAOS cut. MAMBO data are smoothed to  $40''$  here. The core is clearly not symmetrical and  $C^{18}O$  depletion is obvious.

olution to  $24''$  to improve the signal-to-noise ratio. A large hole in emission is visible in the centre of the map. This is due to CO depletion, as is now well established. The PRONAOS strip centered at the  $100\ \mu m$  emission peak came across the most depleted part of the filament. This depletion is also spectacular in terms of spectrum peak temperature (Fig. 3) or integrated intensity (Fig. 4) along the PRONAOS strip. In these figures, the drop of  $C^{18}O$  intensity is correlated with the appearance of  $N_2H^+$ , another sure sign of CO depletion as CO readily destroys  $N_2H^+$  (Bergin & Langer 1997; Caselli 2002; Pagani et al. 2005). To check that the  $C^{18}O$  lines are not dropping for opacity reasons in the centre of the cloud, we observed 3 positions in  $C^{17}O$  (J:1–0). We chose two positions close to the  $C^{18}O$  peaks on each side of the strip ( $\pm 75''$ ) and one in the middle, close to the local minimum of the  $C^{18}O$  emission (Fig. 5). These 3 positions are indicated on Fig. 2 by 3 small white boxes superposed to 3 of the crosses along the PRONAOS strip. Several interesting features are visible:

1. the (0, 0) and ( $+75''$ , 0) offset positions (along the cut) display extremely narrow  $C^{17}O$  and  $C^{18}O$  lines (FWHM = 0.16 to  $0.26\ km\ s^{-1}$  where FWHM stands for full width half maximum).
2. the existence of a velocity gradient across the strip which possibly traces rotation in the  $C^{18}O$  data.
3. the existence of another velocity gradient for  $^{13}CO$  of *opposite* direction.
4. the  $C^{18}O$  (J:1–0) splitting towards the reference position, which is not so much visible in the (J:2–1) line but is clearly so in the  $C^{17}O$  (J:1–0) line, as the dotted lines reveal in Fig. 5.

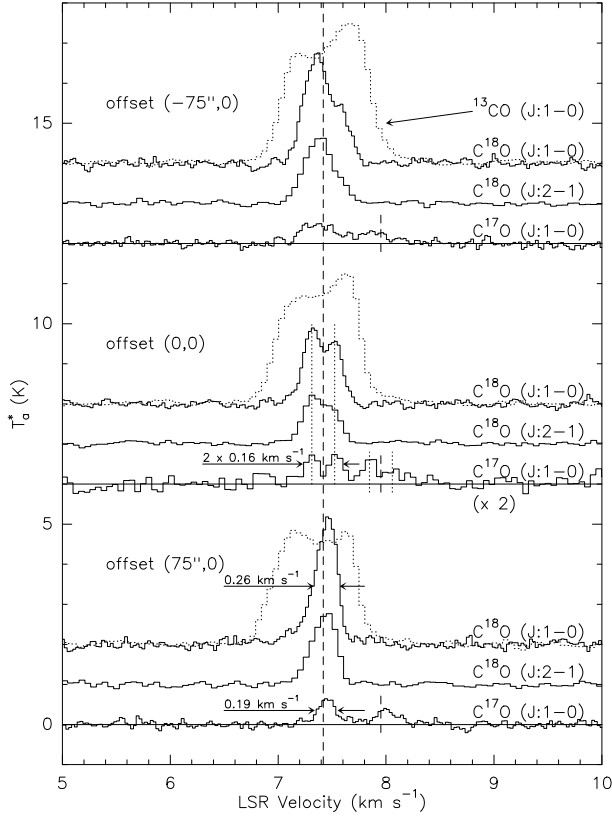
As most of the properties of this cloud change gradually with radius, it is difficult to define what is the core and what is the envelope. One parameter however changes abruptly and this is the velocity field. We will therefore define the envelope as the region where  $^{13}CO$  is revealing a different velocity field from the other species while  $C^{18}O$  and  $N_2H^+$  both trace the core, the outer, undepleted part for the former and the inner depleted one for the latter.

As far as we know, these CO narrow lines are the narrowest  $C^{18}O$  and  $C^{17}O$  lines reported so far, comparable to the very narrow features seen in  $NH_3$  and  $N_2H^+$  in sources like

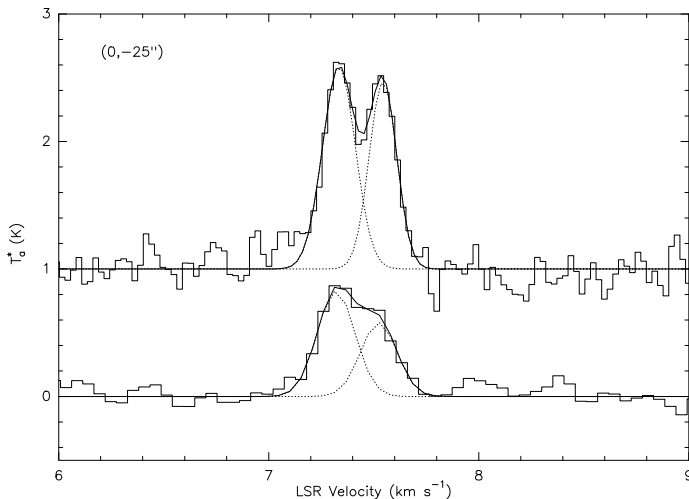
L183 (Pagani et al. 2007). The main difference is that these  $C^{18}O$  and  $C^{17}O$  lines are emitted outside the depleted core, in a region where turbulence is usually still high. The lines are narrow enough so that the  $C^{17}O$   $J_F:1_{7/2}-0_{5/2}$  and  $J_F:1_{3/2}-0_{5/2}$  hyperfine components which are usually blended, are completely separated here.

Figure 6 confirms the extraordinary narrowness of the lines towards the centre of the cloud. These  $C^{18}O$  spectra have been taken at ( $0, -25''$ ) in the frame of the PRONAOS cut, that is ( $-21.6''$ ,  $-12.6''$ ) in the Equatorial J2000 frame. The (J:1–0) spectrum shows clearly two components which we have fitted with 2 independent gaussians. We have also fitted the (J:2–1) spectrum with two unconstrained gaussians. The velocity of each of the two components agree for both lines within the uncertainty of the fit (a difference of  $10\ m\ s^{-1}$  for an uncertainty of 30 and  $40\ m\ s^{-1}$  for the left and right components, respectively). As for  $C^{17}O$  in Fig. 5, the splitting between the two components is  $\sim 200\ m\ s^{-1}$  and the width of the individual components is 150 (right) and 180 (left)  $m\ s^{-1}$ . For a standard gas kinetic temperature of 10 K, for which the optically thin thermal linewidth of CO is  $\sim 0.12\ km\ s^{-1}$ , this sets the turbulent width contribution to the linewidth to  $\lesssim 90\ m\ s^{-1}$ .

If the  $C^{18}O$  and  $C^{17}O$  splitting was due to self-absorption, it would be exactly the reverse, the  $C^{18}O$  (J:2–1) line would have had the deepest self-absorption feature and normally no such feature would have been seen in  $C^{17}O$  since, due to its low abundance and to its hyperfine structure, it is very difficult to make it optically thick. These symmetric features cannot be due to rotational Doppler shifting because for a narrow beam aiming at the rotational axis, most of the material picked up by the beam is moving at right angle to the line of sight having therefore no contribution to the velocity component along it. Only material very near the rotational axis would contribute to the Doppler shifted emission. As the inner core is depleted in CO, such a contribution near the axis is not possible and therefore rotation cannot explain this splitting. To explain this double peak feature, the only possibility left is that the CO envelope is radially moving. The direction of movement (expansion or contraction) can be told from the asymmetry of the  $C^{18}O$  (J:1–0) and (J:2–1) lines. Here, these  $C^{18}O$  lines are stronger in the blue component than in the red component. As we will confirm with the Monte-Carlo model (Sect. 4), this can only be explained by contraction and not expansion despite the absence of heavy self-absorption which is usually invoked to justify blue peaked profiles (Myers et al. 1996). The lines being almost independent due to their narrowness, the blue and red line contributions are emitted from only one side of the cloud each – front or back depending on the movement, expansion or contraction – and have no or very little interaction. The line which comes from the rear part is originating in the backside low density envelope and gets contribution from a material getting denser as the photons travel towards the observer, until they reach the depleted zone and then cross the rest of the cloud without interaction. For a constant kinetic temperature, this means that the excitation temperature of the contributing material is increasing (or remaining constant if thermalized) towards the observer and the successive layers add their contribution to the emergent signal. Conversely, the line formed on the near side of the cloud starts from the highest density and excitation temperature layer, just outside the depleted zone and gets contributions from lesser and lesser dense material with therefore a decreasing excitation temperature. When the excitation temperature decreases, net absorption of photons can happen if opacity is not null. Indeed, the  $C^{18}O$  lines are not really optically thin (opacities are in the range of 0.1 to 0.5) and this



**Fig. 5.** Spectra of  $^{13}\text{CO}$  (dotted lines),  $\text{C}^{17}\text{O}$ , and  $\text{C}^{18}\text{O}$  taken at 3 different positions along the PRONAOS strip: in the middle and close to each side peak  $\text{C}^{18}\text{O}$  emission. The full width at half maximum is indicated for some remarkably narrow lines. Only the  $\text{C}^{17}\text{O}$   $J_{F:17/2}-0_{5/2}$  and  $J_{F:13/2}-0_{5/2}$  are displayed. The dashed line marks the systemic velocity (with an offset of  $+0.534 \text{ km s}^{-1}$  for the  $J_{F:13/2}-0_{5/2}$   $\text{C}^{17}\text{O}$  transition) while the dotted lines for the  $\text{C}^{17}\text{O}$  transition show the symmetrical velocity displacement of each  $\text{C}^{17}\text{O}$  hyperfine component in the (0,0) direction (see text). Lines are artificially offset vertically and the central offset  $\text{C}^{17}\text{O}$  line is multiplied by a factor of 2. The  $\text{C}^{18}\text{O}$  (J:2-1) lines are shown at their original  $11''$  resolution.



**Fig. 6.**  $\text{C}^{18}\text{O}$  (J:1-0) (top) and (J:2-1) (bottom) spectra (histogram plot) taken  $25''$  away from the PRONAOS cut. The total Gaussian fit (full line) for both transitions is shown as well as individual components. The components are separated by  $200 \text{ m s}^{-1}$  and their width is  $150$  (right) and  $180$  (left)  $\text{m s}^{-1}$

is enough to slightly differentiate between the line which comes from the rear part of the cloud which has undergone no attenuation after the highest excitation temperature layer emission and the line which comes from the front part and has suffered from a small absorption due to the outer, less excited layers. The effect is clearly seen towards the (0,0) position: the  $\text{C}^{18}\text{O}$  (J:1-0) line is 20% stronger on the blue side ( $1.81$  and  $1.48 \text{ K}$  peak temperature for the blue and red components, a difference greater than  $10 \sigma$ , with  $\sigma = 27 \text{ mK}$ ), and the  $\text{C}^{18}\text{O}$  (J:2-1) line which due to higher opacity and higher sensitivity to density conditions has lost its red peak (Fig. 5). The red component is therefore the one emitted from the front part of the cloud, the blue component from the rear part and this indicates that the cloud is contracting rather than expanding<sup>10</sup>. The amount of contraction of the  $\text{C}^{18}\text{O}$  core is indicated by the two dotted lines in Fig. 5, namely  $\approx \pm 100 \text{ m s}^{-1}$ . Therefore, the  $\text{C}^{18}\text{O}$  outer core both rotates (from the  $(\pm 75'', 0)$  symmetrical velocity offsets seen in Fig. 5 as mentioned above) and contracts. To our knowledge, this is the first time that core contraction is observed based on  $\text{C}^{18}\text{O}$  and  $\text{C}^{17}\text{O}$  lines.

The  $\text{N}_2\text{H}^+$  hyperfine structure lines do not have such a good signal-to-noise ratio and do not show a structured profile. However, their displacement in velocity along the cut is similar to that of  $\text{C}^{18}\text{O}$  as we can see in Fig. 7.

The  $^{13}\text{CO}$  (J:1-0) line which was observed simultaneously with the  $\text{C}^{18}\text{O}$  (J:1-0) line shows a very different behaviour (Figs. 3, 5, & 7). Its peak intensity is red-shifted and its velocity gradient along the cut is opposite to that of the  $\text{C}^{18}\text{O}$  line. From the large scale  $^{13}\text{CO}$  map obtained with POM-1, we know that the L1506 filament has a width of  $\sim 40'$  in the region around L1506C (Fig. 2). This is  $\sim 6$  times larger than the  $\text{C}^{18}\text{O}$  extent. As we do not know how the  $^{13}\text{CO}$  velocity behaves beyond these central  $6'$ , we cannot claim that this velocity drift is the signature of a rotation of the large scale filament but it definitely indicates that it is opposite to the  $\text{C}^{18}\text{O}$  rotation (Figs. 5 & 7). Similarly, the red peak in the  $^{13}\text{CO}$  velocity profile is probably a sign of gas expansion (Figs. 3 & 5), while  $\text{C}^{18}\text{O}$  is tracing a contraction. *Therefore the extended envelope is dynamically behaving at the opposite of the core.*

Figure 4 shows the dissymmetry of the cloud in both dust and gas. It is remarkable that the  $\text{C}^{18}\text{O}$  lines on each side of the cut have the same maximum integrated intensity despite a variation of 25% in peak intensity. It indicates that the quantity of gas is comparable and that the main reason for the intensity change is the line width difference. It must also be noticed that the  $\text{N}_2\text{H}^+$  integrated intensity profile is strongly asymmetric and varies abruptly at the top, two features we cannot reproduce with our standard one-dimensional (1D) model (see Sect. 4). Its peak position is close to but not coincident with the dust peak position.

We observed the position with the second strongest  $\text{N}_2\text{H}^+$  integrated intensity (offset  $+25''$  along the PRONAOS strip) in

<sup>10</sup> There exists the alternative possibility that the blue peak is stronger than the red peak because of a difference in column densities between front and rear parts of the cloud. If it were the case in such a manner that it would hide the cloud expansion, the difference in column density between the two components would be  $\sim 40\%$  in the optically thin limit (and even more with growing opacity). Indeed, as the intensity difference is about 20% towards the (0,0) position in  $\text{C}^{18}\text{O}$  (J:1-0), it would have to be compensated twice to go from a stronger red component (due to expansion combined with differential excitation) to a weaker red component (as observed) and the effect would be more pronounced for the (J:2-1) component. This possibility seems therefore quite unlikely and even if the two sides of the cloud have different column densities, contraction remains the best explanation.

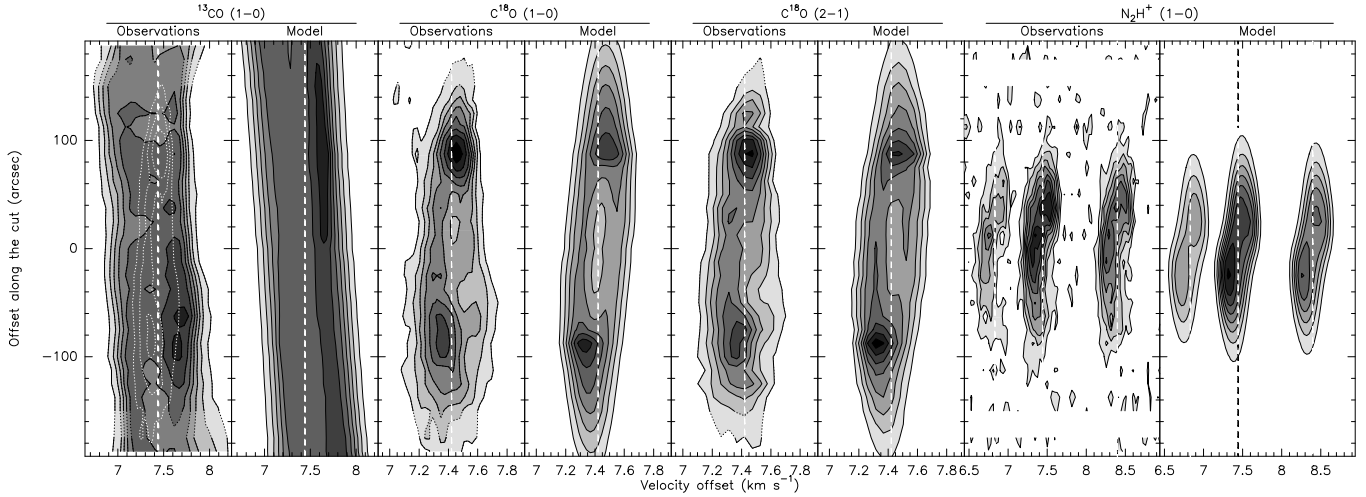


**Fig. 7.** Position-velocity plots along the PRONAOS cut. For each line, we show the observations on the left and the model on the right with the same contour levels. For  $\text{N}_2\text{H}^+$ , we reproduce only the 3 inner hyperfine components. The dashed line marks the systemic velocity of the cloud. For  $^{13}\text{CO}$  and  $\text{C}^{18}\text{O}$  observations, the dotted contours indicate interpolated data (data is missing for offsets  $\pm 162.5''$ ). Superposed to the  $^{13}\text{CO}$  observations, dotted contour levels from the  $\text{C}^{18}\text{O}$  (J:1–0) observation plot are repeated. Only levels 1, 2, and 3 K have been drawn for clarity.

$\text{N}_2\text{D}^+$  (J:1–0) to check the level of deuteration in the inner core (the strongest peak – offset  $+37.5''$  – was identified afterwards). We found only a very weak signal (Fig. 8), the main hyperfine component being only 70 mK. A hyperfine fit was performed using the CLASS fitting routine MINIMIZE with the HFS option<sup>11</sup>.

## 4. Models

### 4.1. density profile

The density radial distribution has been derived from the MAMBO map emission using a Wiener linear inversion method as described by Dupac & Giard (2002). Considering the elongated distribution (along the RA axis), we have modelled the filament with a cylindrical geometry approximation, with its axis in the plane of the sky and perpendicular to the PRONAOS strip, as in Stepnik et al. (2003). We have also taken into account a temperature inward decrease from 15 K down to 8 K. This range has been deduced from the  $A_v$  profile in the filament (Stepnik et al. 2003) combined with the prediction from Zucconi et al. (2001) or Bernard et al. (1992) dust temperature models in cold cores. We have discretized the cylinder into iso-density and iso-temperature rings, and determined the array  $A$  such as:

$$N_{\text{H}_2}(j) = A(i, j) \times n_{\text{H}_2}(i) + b$$

or

$$I_\lambda^j = \sum_i A(i, j) \times B_\lambda(T_i) \times \kappa_{1200 \mu\text{m}} \times m_H \times \mu \times n_{\text{H}_2}(i) + b$$

where (i,j) are respectively the indexes for the rings and the lines of sight,  $N_{\text{H}_2}$  the column density,  $n_{\text{H}_2}(i)$  the gas density in the ring  $i$ ,  $I_\lambda^j$  the observed intensity along the line of sight  $j$ ,  $b$  is the noise level,  $B_\lambda(T_i)$  is the black-body function evaluated for the temperature  $T$  of the ring  $i$ ,  $m_H$  is the proton mass,  $\mu = 2.33$

is the mean molecular weight of interstellar material in molecular clouds and  $\kappa_{1200 \mu\text{m}} = 8 \times 10^{-3} \text{cm}^{-2} \text{g}^{-1}$  is the mass absorption coefficient assumed constant in the core and derived from the dust aggregates emissivity model by Ossenkopf & Henning (1994). The local density  $n_{\text{H}_2}$  in each ring ( $i$ ) is deduced from :  $n_{\text{H}_2} = W \times I_\lambda$ , where we adopt the optimized inversion matrix :

$$W = ({}^t A' \times A')^{-1} \times {}^t A'$$

(cf Dupac & Giard (2002)), with:

$$A' = \kappa_{1200 \mu\text{m}} \times m_H \times A(i, j) \times B_\lambda(T_i)$$

The best optimization has been obtained using a ring thickness value of  $50''$ , and the result leads to an inner density of  $2.4 \times 10^4 \text{cm}^{-3}$  (in average over a  $50''$  radius core).

### 4.2. line modeling

The density profile derived from the dust data has been used as a first guess for our 1D line radiative transfer models but we allowed the profile to be changed because the raw dust map is noisy and its final resolution for the inversion method is only  $50''$  compared to the  $\text{C}^{18}\text{O}$  (J:1–0)  $24''$  and (J:2–1)  $12''$  and because the dust properties are not strongly constrained and can vary, therefore making the derived density uncertain by a factor of 2 typically.

For all three species,  $^{13}\text{CO}$ ,  $\text{C}^{18}\text{O}$ , and  $\text{N}_2\text{H}^+$ , we fit a non-local thermodynamic equilibrium radiative transfer Monte-Carlo model and try to reproduce the spectra (Figs. 9, 10, 11, & 12) and the velocity-position diagram (Fig. 7). The 1D Monte-Carlo model was originally developed by Bernes (1979). It includes microscopic turbulence and a radial velocity field. It was subsequently modified to include rotation (Pagani & Breart de Boisanger 1996) and a variant was developed to treat the hyperfine structure of  $\text{N}_2\text{H}^+$  (Pagani et al. 2007). The 1D cloud parameters are shown in Table 2 and the species abundances are traced as a function of radius in Fig. 13. Here the model is spherical, with a radius equal to the dust cylinder radius and with the rotation axis similar to the cylinder

<sup>11</sup> <http://www.iram.fr/IRAMFR/GILDAS/>

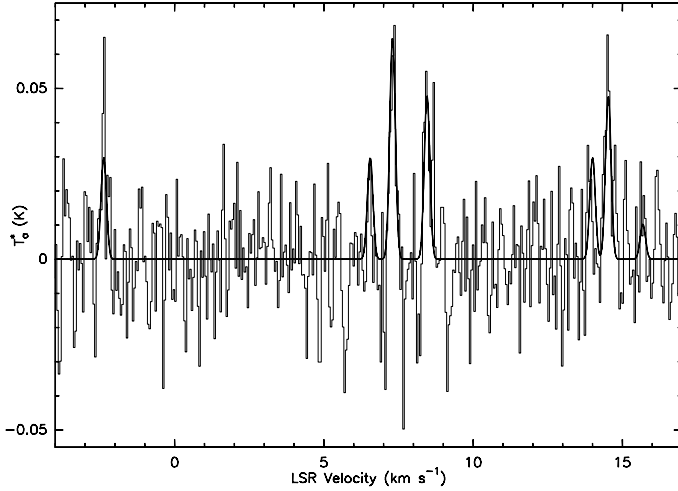


**Fig. 8.** Spectrum of  $\text{N}_2\text{D}^+$  taken at offset  $+25''$  along the PRONAOS strip. The hyperfine fit is superposed to the data. The data is Hanning smoothed once. The sampling is  $50 \text{ m s}^{-1}$  and the rms is  $13 \text{ mK}$ .

axis of the dust model, i.e. supposed to be aligned with the embedding filament elongation and therefore perpendicular to the PRONAOS strip. The model data to be compared to the observations are taken at the equator considered to be a good approximation of a cylinder slice, as already discussed in Pagani et al. (2007) for a similar case. For the  $^{13}\text{CO}$  emission, as our high spatial and velocity resolution strip only extends upon  $6'$  and because the  $^{13}\text{CO}$  line is optically thick and much more extended, it is difficult to build a simple 1D model to reproduce and constrain the  $30\text{-m } ^{13}\text{CO}$  observations (the POM-1 data are too coarse and too noisy for this purpose). More generally, the cloud is not symmetrical and therefore our 1D Monte-Carlo model cannot reproduce the various differences between positive and negative offsets. However, we have tried to fit globally the observations and overall to use a similar cloud description for the  $\text{N}_2\text{H}^+$  and  $\text{C}^{18}\text{O}$  line models. Though the  $^{13}\text{CO}$  data are too difficult to reproduce with the 1D Monte-Carlo code, we have attempted to fit them as well, at least to get some estimate of the physical conditions in the outer parts which could explain the observations. From the  $\text{C}^{18}\text{O}$  and  $\text{N}_2\text{H}^+$  data, we find that the cloud rotational axis could also be slightly offset along the PRONAOS cut (about  $+12''$ ) with respect to our reference position (which was set somewhat arbitrarily). The peak  $\text{N}_2\text{H}^+$  integrated intensity is even further away from the reference position ( $+37.5''$ ) but setting the rotational axis that far does not fit with the overall velocity profile. Despite the fact that the cloud extension on the positive offset side is smaller than on the negative offset side, the fit is relatively good, especially towards the centre of the cloud. As mentioned above, we have tried to somewhat adjust the density profile and found a solution which is close to Tafalla et al. (2002) formula for the  $\text{N}_2\text{H}^+ - \text{C}^{18}\text{O}$  region :

$$n(\text{H}_2) = \frac{n_0(\text{H}_2)}{1 + \left(\frac{r}{r_0}\right)^\alpha} \text{ cm}^{-3} \quad (1)$$

with  $n_0(\text{H}_2) = 5 \times 10^4 \text{ cm}^{-3}$ ,  $r_0 = 1 \times 10^4 \text{ A.U.}$  and  $\alpha = 2.5$ . This profile provides a peak dust emission comparable to the MAMBO observation, and the average density of  $\sim 4 \times 10^4 \text{ cm}^{-3}$  in a  $50''$  radius is within a factor of 2 of the peak density derived from the MAMBO observations. Apart from the dust properties which are not strongly constrained, an equivalently possible ex-

planation for this factor of  $\lesssim 2$  difference is that the  $\text{He} + \text{N}_2\text{H}^+$  collisional coefficients we presently use (Daniel et al. 2005) are overestimating the true  $\text{H}_2$  density needed to collisionally excite the  $\text{N}_2\text{H}^+$  to its  $J = 1$  level as discussed in Pagani et al. (2007). From dust and  $\text{N}_2\text{H}^+$  measurements, we find that the density in this core is rather low, a factor of 2 to 4 below the threshold proposed by Keto & Caselli (2008) for prestellar cores. Therefore, it is not such a core.

The  $\text{CO} + \text{N}_2\text{H}^+$  model which we present here is by no means unique but represents a family of possible solutions. They have remarkable features which are common to all of them:

1. a peak column density of  $N(\text{H}_2) \approx 2 \times 10^{22} \text{ cm}^{-2}$ , equivalent to  $A_V \approx 20 \text{ mag}$  (following Bohlin et al. 1978). This is low compared to most other cases with similar strong  $\text{C}^{18}\text{O}$  depletion but slightly higher than in L1498 which has a peak column density of  $N(\text{H}_2) \approx 1.3 \times 10^{22} \text{ cm}^{-2}$  (Shirley et al. 2005)<sup>12</sup>.
2. a strong central depletion ( $\geq 30$ ) of  $\text{C}^{18}\text{O}$ .
3.  $\text{C}^{18}\text{O}$  depletion starting at a density between  $1.5$  and  $2 \times 10^4 \text{ cm}^{-3}$ .
4. for both the  $\text{C}^{18}\text{O}$  lines (towards the positive offsets) and the  $\text{N}_2\text{H}^+$  line (for all offsets), the linewidth is so narrow that the turbulence contribution to the width is negligible and is set to  $V_{\text{turb}}(\text{FWHM}) \leq 68 \text{ m s}^{-1}$ . This is the lowest turbulence reported for  $\text{C}^{18}\text{O}$  lines to our knowledge. The line width is mostly dominated by the thermal width and the enlargement due to macroscopic kinematics (rotation and infall).
5. the radial velocity is strongly constrained in the  $\text{C}^{18}\text{O}$  envelope but not so much in the  $\text{N}_2\text{H}^+$  internal part. However, a constant infall around  $0.1 \text{ km s}^{-1}$  is compatible with the data. No infall is not.
6. the rotational velocity is decreasing with increasing radius. Solid rotation is therefore excluded and velocity dependences of the type  $V \propto r^{-\alpha}$  with  $\alpha \approx 0.5$  gave good solutions.
7. the temperature pattern requests a slightly higher temperature in the  $\text{N}_2\text{H}^+$  inner core ( $\sim 10 \text{ K}$ ) than in the  $\text{C}^{18}\text{O}$  outer core ( $\sim 8 \text{ K}$ ). If correct this would be similar to the B68 case (Bergin et al. 2006).

The  $\text{C}^{18}\text{O}$  temperature is determined by the necessity to fit both the  $(J:1-0)$  and  $(J:2-1)$  lines with a relatively constrained dust profile while the  $\text{N}_2\text{H}^+$  temperature is the minimum we could get trying to minimize also the needed density. Despite the observation of a single transition for  $\text{N}_2\text{H}^+$ , we are constrained by the hyperfine structure (Pagani et al. 2007, see ). However this temperature difference could possibly prove to be inaccurate if the actual  $\text{H}_2 - \text{N}_2\text{H}^+$  collisional coefficients were available: they are expected to be higher than the present  $\text{He} - \text{N}_2\text{H}^+$  ones and therefore would probably allow to fit the observations with both a lower temperature and a lower density. In any case, the gas appears cooler than what Stepnik et al. (2003) have found for the dust ( $\sim 12 \text{ K}$ ). Either their resolution is too coarse and mix up a large fraction of the (warmer) envelope emission with the core emission, or their single temperature fit is too simple by lack of constraints (we have shown that in the case of L183 cold core the  $200 \mu\text{m}$  emission is not tracing the same dust as the submm emission and that a temperature gradient is compulsory, Pagani et al. 2004) or, finally the gas and the dust being

<sup>12</sup> Note that Shirley et al. (2005) disagree on the total dust amount and peak density of L1498 with respect to what Tafalla et al. (2004) find. If we follow the latter, L1498 is closer to a normal prestellar core than to a simple core. The discrepancy has only partly been explained by Shirley et al. (2005).

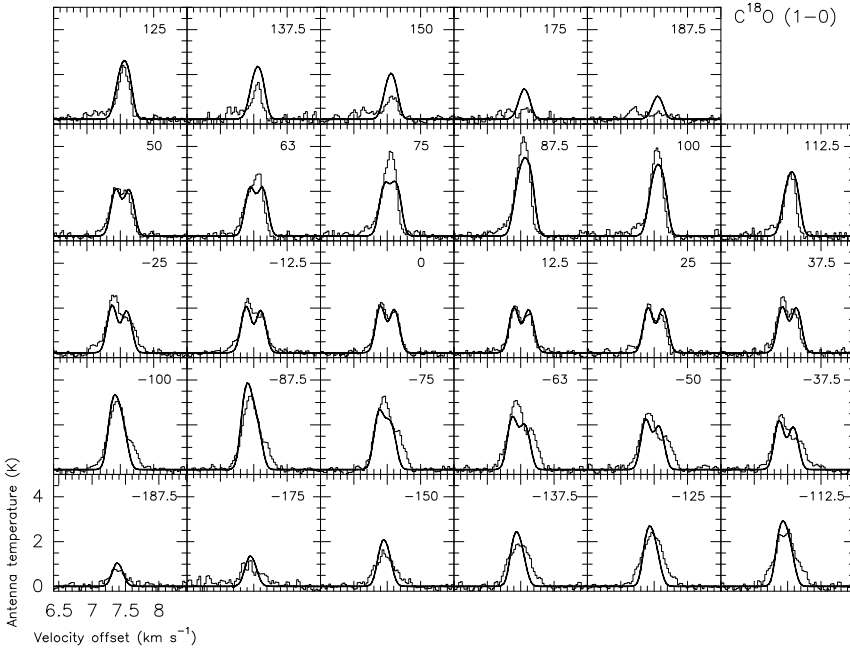


**Fig. 9.** Fit of the individual  $\text{C}^{18}\text{O}$  ( $J:1-0$ ) spectra along the PRONAOS cut. The histogram plot represents the data, the thick continuous curve, the model. A FWHM turbulent velocity of  $0.11 \text{ km s}^{-1}$  has been used all over the cut which explains why the model lines are larger than the observations for the positive offsets. Offsets along the PRONAOS cut in arcseconds are given in the upper right corner of each spectrum.

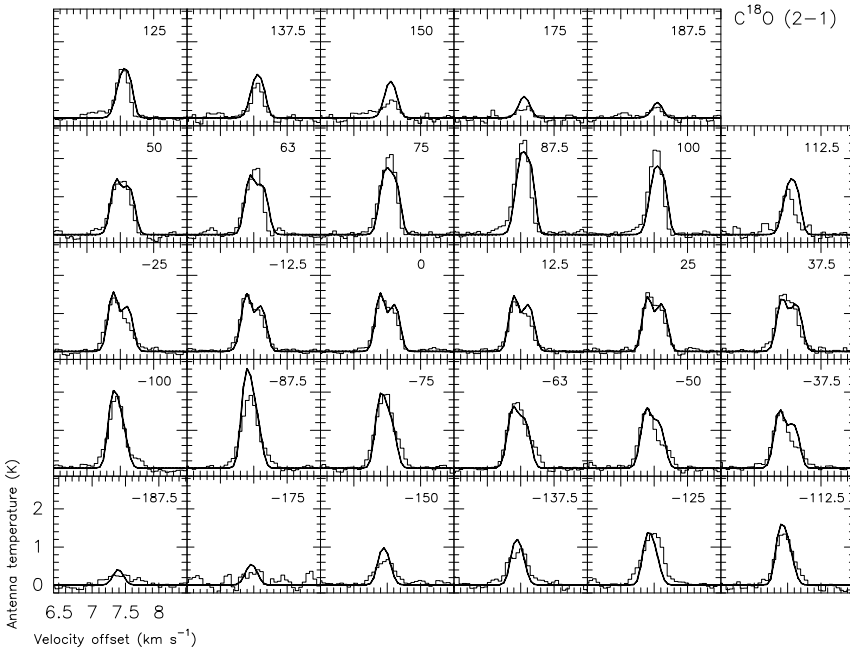


**Fig. 10.** Same as Fig. 9 for  $\text{C}^{18}\text{O}$  ( $J:2-1$ ) spectra.

decoupled at these low densities ( $n(\text{H}_2) \leq 5 \times 10^4 \text{ cm}^{-3}$  or less), the dust could be warmer than the gas though this is not usually expected.

The modeling of the  $\text{N}_2\text{D}^+$  ( $J:1-0$ ) line indicates a column density of 4 to  $8 \times 10^{11} \text{ cm}^{-2}$ , depending on the chosen  $\text{N}_2\text{D}^+$  abundance profile which we cannot constrain with only one observation. The peak  $\text{N}_2\text{H}^+$  column density is  $\sim 2 \times 10^{13} \text{ cm}^{-2}$  and therefore the deuterium enrichment is 2–4%. Compared to L183 (Pagani et al. 2007, 2009b), we find a similar deuteration level at similar densities indicating that the evolutionary speed of the deuterium enrichment is probably similar and therefore can be used to determine the age of the core.

Beyond the core characterized by  $\text{C}^{18}\text{O}$  narrow lines, the envelope, as traced by  $^{13}\text{CO}$ , is best described with an almost constant density (in the range  $200\text{--}1000 \text{ cm}^{-3}$ ) and a large turbulence ( $V_{\text{turb}}(\text{FWHM}) = 0.4 \text{ km s}^{-1}$ ). To follow its macroscopic velocity drift we had to introduce a counter-rotating pattern in the external layers set constant to  $-0.3 \text{ km s}^{-1}$ . We do not claim that the  $^{13}\text{CO}$  is indeed rotating but this is the only way to approach the velocity profile of this line with our model. Similarly, to reproduce the redshifted peak, we had to introduce an expansion velocity of  $90 \text{ m s}^{-1}$ , that is comparable in amplitude to the infall velocity of the core. The fit is not perfect inasmuch as we could not centre the peak emission in our model at the same position as in the observed position-velocity diagram (Fig. 7) but



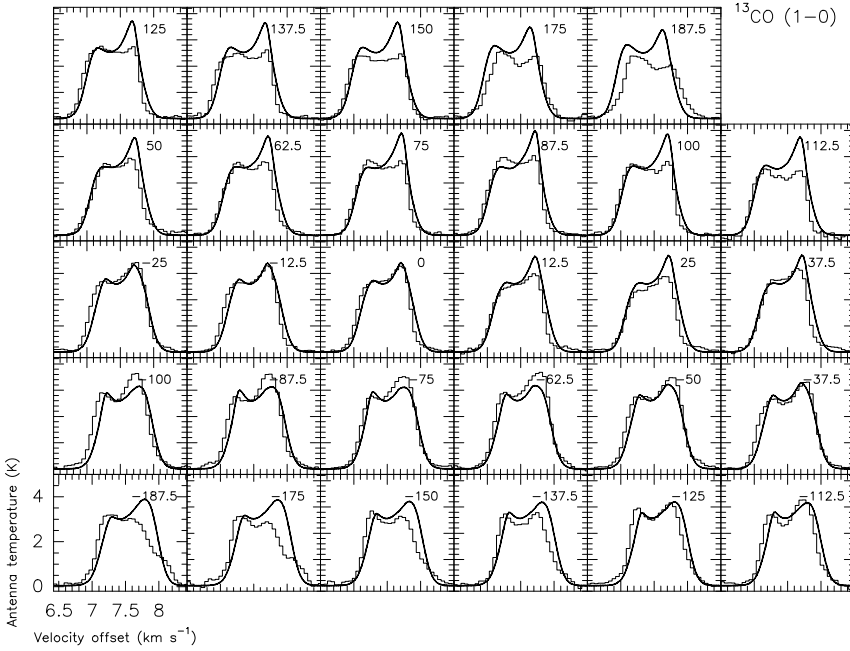


**Fig. 11.** Fit of the individual  $^{13}\text{CO}$  ( $J:1-0$ ) spectra along the PRONAOS cut. The histogram plot represents the data, the thick continuous curve, the model.

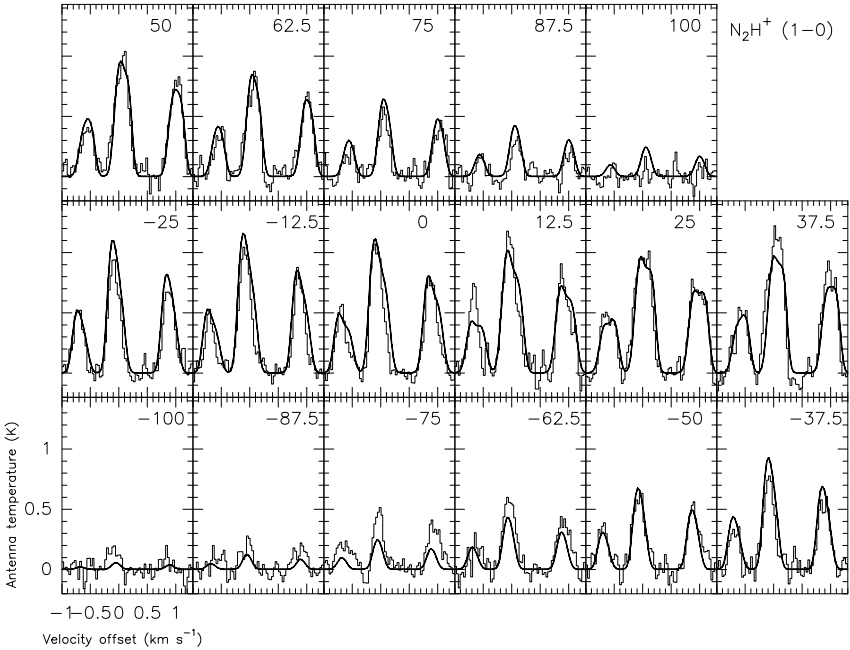


**Fig. 12.** Fit of the individual  $\text{N}_2\text{H}^+$  ( $J:1-0$ ) spectra along the PRONAOS cut. The histogram plot represents the data, the thick continuous curve, the model. Only the 3 central hyperfine structure components are displayed. A turbulent velocity of  $0.068 \text{ km s}^{-1}$  has been used.

the fit bears some resemblance with the reality as shown also in Fig. 11. The derived parameters are therefore reasonably close to the actual situation and this envelope is clearly decoupled from the core in terms of density profile as much as in terms of turbulence and large scale motions. That region is also marked by a very high abundance of  $^{13}\text{CO}$  ( $6 \times 10^{-6}$ ) and the absence of  $\text{C}^{18}\text{O}$  ( $< 5 \times 10^{-9}$ , an abundance of  $1 \times 10^{-8}$  is marginally consistent with the observations). The density is not well constrained in the external envelope but as the  $^{13}\text{CO}$  abundance is already high (standard value is  $1-2 \times 10^{-6}$ , i.e. 3 to 6 times less), the density cannot be lower than what we have assumed here as a lower density would increase even more the  $^{13}\text{CO}$  abundance. Conversely, we could increase the density to lower the abundance of  $^{13}\text{CO}$ , but it would become higher than the density in the last  $\text{C}^{18}\text{O}$  layers. In the absence of other  $^{13}\text{CO}$  transitions it is difficult to constrain correctly the density and the abundance in these last, turbulent layers.

The collapsing core has a size of  $\sim 3 \times 10^4$  AU in radius and holds a mass of  $\sim 4 M_{\odot}$ . This size is larger than the one of L1498 which was already shown to be the largest by 50% among the nearby prestellar cores mentioned in the study by Shirley et al. (2005). Our mass estimate is somewhat approximate as the density of the  $\text{N}_2\text{H}^+$  region is possibly overestimated but on the other hand, the core could be slightly more extended than a sphere, closer to a cylinder. The estimate derived from the dust observations is similar but less constrained due to the unknowns on the dust emissivity and temperature in the core at scales smaller than the PRONAOS resolution. The  $^{13}\text{CO}$  low density filament holds at least  $20 M_{\odot}$  accounting only for the part along its main axis which covers the core. Its diameter is 250,000 A.U. or 1.25 pc.

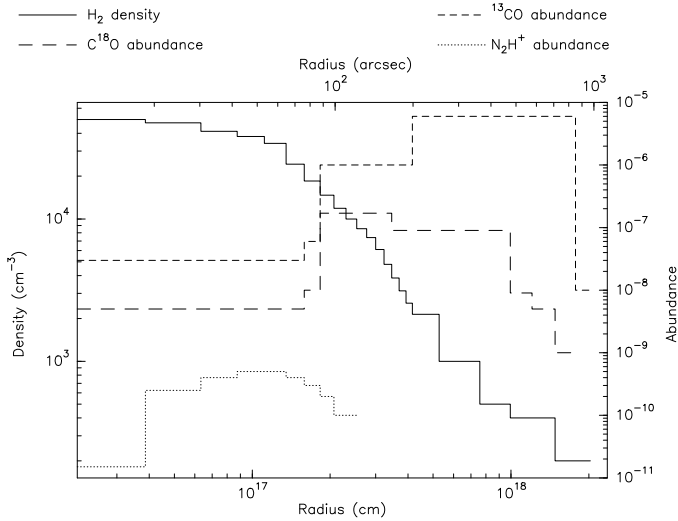
**Table 2.** The Monte-Carlo cloud model used to fit the spectra (Figs. 7, and 9 – 12)

Shell Radius (A.U.)	Shell Radius ( $''$ )	Density ( $\text{cm}^{-3}$ )	Temperature (K)	Rad.velocity <sup>a</sup> ( $\text{km s}^{-1}$ )	Rot.velocity ( $\text{km s}^{-1}$ )	Turbulence <sup>b</sup> ( $\text{km s}^{-1}$ )	Abundance <sup>c</sup>		
							$\text{N}_2\text{H}^+$	$\text{C}^{18}\text{O}$	$^{13}\text{CO}$
1740	12	50000	10	0.11	0.200	$\leq 0.11 / \leq 0.068$	1.5(-11)	$\leq 5(-9)$	$\leq 3(-8)$
3480	25	47400	10	0.11	0.141	$\leq 0.11 / \leq 0.068$	2.5(-10)	$\leq 5(-9)$	$\leq 3(-8)$
5220	37	41300	10	0.11	0.115	$\leq 0.11 / \leq 0.068$	4(-10)	$\leq 5(-9)$	$\leq 3(-8)$
6933	50	38100	10	0.11	0.100	$\leq 0.11 / \leq 0.068$	5(-10)	$\leq 5(-9)$	$\leq 3(-8)$
8666	62	33900	10	0.11	0.089	$\leq 0.11 / \leq 0.068$	5(-10)	$\leq 5(-9)$	$\leq 3(-8)$
10400	75	24300	10	0.11	0.082	$\leq 0.11 / \leq 0.068$	4(-10)	$\leq 5(-9)$	$\leq 3(-8)$
12133	87	18500	10	0.11	0.076	$\leq 0.11 / \leq 0.068$	3(-10)	1(-8)	6(-8)
13933	100	14700	10	0.11	0.070	$\leq 0.11 / \leq 0.068$	2(-10)	1.7(-7)	1(-6)
15666	112	11900	9	0.11	0.066	$\leq 0.11 / \leq 0.068$	1(-10)	1.7(-7)	1(-6)
17400	125	9990	8	0.11	0.063	$\leq 0.11 / \leq 0.068$	1(-10)	1.7(-7)	1(-6)
19133	137	8540	8	0.11	0.060	$\leq 0.11 / \leq 0.068$		1.7(-7)	1(-6)
20866	150	7400	8	0.11	0.058	$\leq 0.11 / \leq 0.068$		1.7(-7)	1(-6)
22600	162	6100	8	0.11	0.055	$\leq 0.11 / \leq 0.068$		1.7(-7)	1(-6)
24333	175	4800	8	0.11	0.053	$\leq 0.11 / \leq 0.068$		1.7(-7)	1(-6)
26066	187	3850	8	0.11	0.052	$\leq 0.11 / \leq 0.068$		1.7(-7)	1(-6)
27866	200	3130	8	0.11	0.050	$\leq 0.11 / \leq 0.068$		1.7(-7)	1(-6)
29600	212	2560	8	0.11	0.048	$\leq 0.11 / \leq 0.068$		1.7(-7)	1(-6)
31333	225	2140	8	0	-0.3	0.4		$\leq 5(-9)$	6(-6)
46666	335	1000	8	-0.09	-0.3	0.4		$\leq 5(-9)$	6(-6)
66666	479	500	10	-0.09	-0.3	0.4		$\leq 5(-9)$	6(-6)
83333	598	400	12	-0.09	-0.3	0.4		$\leq 5(-9)$	6(-6)
100000	718	400	13	-0.09	-0.3	0.4		$\leq 5(-9)$	6(-6)
126666	909	200	13	-0.09	-0.3	0.4		$\leq 1(-9)$	1(-8)

<sup>a</sup> positive velocity indicates inward motion (contraction).

<sup>b</sup> FWHM turbulence is  $\leq 0.068 \text{ km s}^{-1}$  for the positive offsets in the  $\text{C}^{18}\text{O}$  model and for all offsets in the  $\text{N}_2\text{H}^+$  model and  $\leq 0.11 \text{ km s}^{-1}$  otherwise (for Figs. 9 and 10 only one value could be used:  $0.11 \text{ km s}^{-1}$  has been selected).

<sup>c</sup> relative to  $\text{H}_2$ . 1(-10) means  $1 \times 10^{-10}$ .

**Fig. 13.**  $\text{H}_2$  density and molecular abundance (relative to  $\text{H}_2$ ) as a function of radius.

## 5. Discussion

Several aspects of this part of the L1506 filament are surprising and presently difficult to explain. The expanding and counter-drifting external envelope is one of them. One partially similar case has however already been reported: Young et al. (1981) have shown that the B5 core as traced by  $\text{C}^{18}\text{O}$  had a position/velocity profile gradient opposite to the  $^{12}\text{CO}$  one which they interpreted as a counter-rotating core (but they don't discuss the radial component). Contemporary theoretical work (Gillis et al. 1979; Mouschovias & Paleologou 1979) was in-

voked to explain this situation: a radial, frozen-in magnetic field perpendicular to the rotation axis could brake down the rotation of the cloud but because the field remains anchored to the external regions, the magnetic torques do not vanish immediately and counter-rotation is induced in the core which could oscillate several times before coming to a halt. Whether this is a similar case here is not yet clear because 1) we are not certain that the  $^{13}\text{CO}$  itself is tracing a rotation, 2) the expansion of the  $^{13}\text{CO}$  envelope is not predicted by the model and, 3) we know nothing about the magnetic field inside this core (external parts have been mapped though, Moneti et al. 1984; Heiles 2000).

The strong depletion of  $\text{C}^{18}\text{O}$  with its abrupt appearance at relatively low density is another one. It is similar to the L1498 case but in sheer contrast with other very young cores, like L1495B, L1521B, and L1521E which show no depletion despite a density which is typically 5 times higher (and possibly 10 times if  $\text{He-N}_2\text{H}^+$  collisional coefficients are indeed over-evaluating the actual density in L1506C or if we compare to L1498 peak density as derived by Shirley et al. 2005). Based mainly on this absence of depletion, these cores have been judged to be young but it is somewhat strange that having very recently acquired their present density state, they show no kinematical sign of contraction. It is thus conceivable that they are older than assumed and that the absence of depletion could be due to another mechanism, like a strong desorption, an ill-understood mechanism (Roberts et al. 2007). Indeed, it is thought that energetic cosmic ray impacts can desorb the most volatile ices like CO (Leger et al. 1985; Hasegawa & Herbst 1993; Branga & Johnson 2004; Roberts et al. 2007). The desorption efficiency is inversely correlated to the size of the grains as smaller grains are easier to warm up. Therefore the question arises whether cores like L1495B have smaller grains than L1506C or not and how much

different in size should these grains be to allow or prevent an efficient desorption of CO. As explained by Roberts et al. (2007), all the desorption mechanisms are yet poorly known and it is presently difficult to go further. However, if this explanation proves to be valid, then one has to understand why grains coagulate in some sources and not in others. Turbulence could be one of the main key parameters involved in this differentiation between cores. From Chokshi et al. (1993) and Poppe & Blum (1997) works, Flower et al. (2005) show that dust coagulation efficiency peaks for turbulent velocities in the range  $10 - 80 \text{ m s}^{-1}$  (see their Fig. A.1), a condition that is hardly met even in the most quiescent prestellar cores but fits the present case. On the opposite, L1521E shows no depletion while the turbulence is suprathreshold (even for  $\text{N}_2\text{H}^+$ ,  $V_{\text{turb}}(\text{FWHM}) = 0.27 \text{ km s}^{-1}$ , Tafalla & Santiago 2004, a factor of 4 at least larger than in L1506C). If the size of the grains in L1521E is not known, large grains have been advocated to explain sub-millimeter emission in L1506C: Stepnik et al. (2003) have built a model where the very small grains, emitting at  $60 \mu\text{m}$ , disappear for offsets lower than  $r_0 = 4'$  from the centre while the sub-mm emissivity increases by a factor of 3.4 due to the formation of fluffy aggregates. Their observations were taken with an angular resolution of  $2-3.5''$ , so the value of  $r_0$  could be lower and fit the extent ( $\pm 200''$ ) of the low turbulence region in L1506C. Grain growth, depletion and desorption are certainly not completely understood at the moment.

The absence of  $\text{C}^{18}\text{O}$  on 5/6th of the external envelope width as traced by the POM-1  $^{13}\text{CO}$  observations is another puzzle. The  $^{13}\text{CO}$  abundance itself seems to be higher than usual so that the  $^{13}\text{CO}/\text{C}^{18}\text{O}$  ratio reaches 600–1200 over a large region. Though  $^{13}\text{CO}$  fractionation does exist, it is weak and does not seem to be able to explain this difference. More observations of the envelope (including  $^{13}\text{CO}$  (J:1–0) and (J:2–1) and very low noise  $\text{C}^{18}\text{O}$  transitions) are needed to address this issue.

Clear trace of collapse among prestellar cores has been found in a few cases. Lee et al. (1999, 2004) observed a large number of asymmetrically blue profiles towards a sample of starless cores but they traced the CS kinematics with respect to  $\text{N}_2\text{H}^+$  or  $\text{DCO}^+$  and, as CS is depleted inside the  $\text{N}_2\text{H}^+$  region, they trace the inward motion of the envelope only. A few prestellar cores are indeed modeled with a collapsing core, the best studied one being L1544 (e.g. Williams et al. 1999; Tafalla et al. 2002; van der Tak et al. 2005) which was reported to clearly undergo a collapse from line profile fitting. Tafalla et al. (2004) also invoke the possibility of infall from the observations of two other cores, L1498 and L1517B despite the absence of a clear velocity gradient and Williams et al. (2006) found that L694-2 has a profile reminiscent of L1544, indicating also probable infall. This has been confirmed by Lee et al. (2007) who also report infall of L1197. Here the inward motion of  $\text{N}_2\text{H}^+$  is not strongly constrained in amplitude but unavoidable to reproduce the velocity-profile plot: no infall at all gives clearly a wrong result but the details of the radial velocity profile are uncertain. The inward motion is also clearly shown by the  $\text{C}^{18}\text{O}$  and  $\text{C}^{17}\text{O}$  lines. It is the first time to our knowledge that such lines do trace the collapse of a core. We think that this is possible here because several favorable factors are met:

1. no CO isotopologues in the central part, separating clearly the front and rear moving layers as indicated by  $\text{C}^{17}\text{O}$ .
2. no  $\text{C}^{18}\text{O}$  in the extended envelope which would have hidden or blurred the faint variation of intensity between the blue and red emissions which let us differentiate between expansion and contraction

3. low  $\text{C}^{18}\text{O}$  velocity dispersion, increasing the line opacity near unity ( $\tau_{J:1-0} = 0.56$ ,  $\tau_{J:2-1} = 0.91$ ). Combined with the outward decreasing excitation temperature, it allows for the weak but measurable differential absorption between the blue and red components.

The most surprising aspect is that this core with a density below  $\sim 1 \times 10^5 \text{ cm}^{-3}$  is supposed to be dynamically stable given its total mass (less than  $10 M_{\odot}$ , Keto & Caselli 2008) which is clearly not the case here (the core mass being estimated to be  $\sim 4 M_{\odot}$ ). However, as noted by Keto & Caselli (2008), most clouds without non-thermal energy support would be unstable and in this case, turbulence is abnormally low, non-measurable in several parts of the core. This would support the idea of a possible collapse though we have no clue on the magnetic field intensity and direction. If a magnetic field is indeed present to induce the core counter-rotation, it is not incompatible with infall as it is included in the magnetic braking model of Mouschovias & Paleologou (1979). Oscillations or sound waves have been invoked in the case of e.g. B68 (Maret et al. 2007) and one could be tempted to invoke a similar argument here but the rotation of  $\text{C}^{18}\text{O}$  and "counter-rotation" of  $^{13}\text{CO}$  seem difficult to explain by sound waves.

## 6. Conclusions

The large size of L1506C and its low density clearly indicate that it is not yet a prestellar core but its inward motion and its kinematical decoupling with the outer envelope are signs that it is in the process of turning into one. It is the first time that a low density core is clearly observed to collapse to form a prestellar core, both the kinematical and density status of L1498 being somewhat unclear. Two different evolutionary paths from normal clouds to prestellar cores seem to exist: one which starts with density enhancement first much before any depletion occurs and one which starts with depletion first. Two questions arise: what is the reason for this differentiation (turbulence via its action on grain growth, itself limiting the desorption capability of cosmic rays?) and are both paths really leading to standard prestellar cores? Coming observations with the Herschel Space Observatory will help to address these questions and the nature of the dust inside this object.

*Acknowledgements.* We want to thank an anonymous referee for her/his fruitful comments which helped to improve the manuscript and P.F. Goldsmith for fruitful discussions.

## References

- Abergel, A., Boulanger, F., Mizuno, A., & Fukui, Y. 1994, *ApJ*, 423, L59  
 Bergin, E. A. & Langer, W. D. 1997, *ApJ*, 486, 316  
 Bergin, E. A., Maret, S., van der Tak, F. F. S., et al. 2006, *ApJ*, 645, 369  
 Bernard, J. P., Boulanger, F., Desert, F. X., & Puget, J. L. 1992, *A&A*, 263, 258  
 Bernes, C. 1979, *A&A*, 73, 67  
 Bohlin, R. C., Savage, B. D., & Drake, J. F. 1978, *ApJ*, 224, 132  
 Bringa, E. M. & Johnson, R. E. 2004, *ApJ*, 603, 159  
 Caselli, P. 2002, *Planet. Space Sci.*, 50, 1133  
 Chokshi, A., Tielens, A. G. G. M., & Hollenbach, D. 1993, *ApJ*, 407, 806  
 Daniel, F., Dubernet, M.-L., Meuwly, M., Cernicharo, J., & Pagani, L. 2005, *MNRAS*, 363, 1083  
 Dupac, X. & Giard, M. 2002, *MNRAS*, 330, 497  
 Elias, J. H. 1978, *ApJ*, 224, 857  
 Flower, D. R., Pineau Des Forêts, G., & Walmsley, C. M. 2005, *A&A*, 436, 933  
 Gillis, J., Mestel, L., & Paris, R. B. 1979, *MNRAS*, 187, 311  
 Hasegawa, T. I. & Herbst, E. 1993, *MNRAS*, 261, 83  
 Heiles, C. 2000, *AJ*, 119, 923  
 Hirota, T., Ito, T., & Yamamoto, S. 2002, *ApJ*, 565, 359  
 Hirota, T., Maezawa, H., & Yamamoto, S. 2004, *ApJ*, 617, 399

- Kenyon, S. J., Dobrzycka, D., & Hartmann, L. 1994, *AJ*, 108, 1872
- Keto, E. & Caselli, P. 2008, *ApJ*, 683, 238
- Klapper, G., Surin, L., Lewen, F., et al. 2003, *ApJ*, 582, 262
- Lada, C. J., Huard, T. L., Crews, L. J., & Alves, J. F. 2004, *ApJ*, 610, 303
- Lee, C. W. & Myers, P. C. 1999, *ApJS*, 123, 233
- Lee, C. W., Myers, P. C., & Plume, R. 2004, *ApJS*, 153, 523
- Lee, C. W., Myers, P. C., & Tafalla, M. 1999, *ApJ*, 526, 788
- Lee, S. H., Park, Y.-S., Sohn, J., Lee, C. W., & Lee, H. M. 2007, *ApJ*, 660, 1326
- Leger, A., Jura, M., & Omont, A. 1985, *A&A*, 144, 147
- Maret, S., Bergin, E. A., & Lada, C. J. 2007, *ApJ*, 670, L25
- Moneti, A., Pipher, J. L., Helfer, H. L., McMillan, R. S., & Perry, M. L. 1984, *ApJ*, 282, 508
- Mouschovias, T. C. & Paleologou, E. V. 1979, *ApJ*, 230, 204
- Myers, P. C., Mardones, D., Tafalla, M., Williams, J. P., & Wilner, D. J. 1996, *ApJ*, 465, L133+
- Nercessian, E., Castets, A., Benayoun, J. J., & Cernicharo, J. 1988, *A&A*, 189, 207
- Onishi, T., Mizuno, A., Kawamura, A., Ogawa, H., & Fukui, Y. 1996, *ApJ*, 465, 815
- Ossenkopf, V. & Henning, T. 1994, *A&A*, 291, 943
- Pagani, L., Bacmann, A., Cabrit, S., & Vastel, C. 2007, *A&A*, 467, 179
- Pagani, L., Bacmann, A., Motte, F., et al. 2004, *A&A*, 417, 605
- Pagani, L. & Breart de Boisanger, C. 1996, *A&A*, 312, 989
- Pagani, L., Daniel, F., & Dubernet, M.-L. 2009a, *A&A*, 494, 719
- Pagani, L., Pardo, J.-R., Apponi, A. J., Bacmann, A., & Cabrit, S. 2005, *A&A*, 429, 181
- Pagani, L., Vastel, C., Hugo, E., et al. 2009b, *A&A*, 494, 623
- Poppe, T. & Blum, J. 1997, *Advances in Space Research*, 20, 1595
- Roberts, J. F., Rawlings, J. M. C., Viti, S., & Williams, D. A. 2007, *MNRAS*, 382, 733
- Shirley, Y. L., Nordhaus, M. K., Greevich, J. M., et al. 2005, *ApJ*, 632, 982
- Stepnik, B., Abergel, A., Bernard, J.-P., et al. 2003, *A&A*, 398, 551
- Tafalla, M., Myers, P. C., Caselli, P., & Walmsley, C. M. 2004, *A&A*, 416, 191
- Tafalla, M., Myers, P. C., Caselli, P., Walmsley, C. M., & Comito, C. 2002, *ApJ*, 569, 815
- Tafalla, M. & Santiago, J. 2004, *A&A*, 414, L53
- van der Tak, F. F. S., Caselli, P., & Ceccarelli, C. 2005, *A&A*, 439, 195
- Willacy, K., Langer, W. D., & Velusamy, T. 1998, *ApJ*, 507, L171
- Williams, J. P., Lee, C. W., & Myers, P. C. 2006, *ApJ*, 636, 952
- Williams, J. P., Myers, P. C., Wilner, D. J., & di Francesco, J. 1999, *ApJ*, 513, L61
- Young, J. S., Goldsmith, P. F., Langer, W. D., & Wilson, R. W. 1981, *ApJ*, 251, L81
- Zucconi, A., Walmsley, C. M., & Galli, D. 2001, *A&A*, 376, 650

## List of Objects

- 'L1506' on page 1
- 'L1506C' on page 1
- 'B68' on page 1
- 'L183' on page 1
- 'L1498' on page 1
- 'L1544' on page 1
- 'L1495B' on page 1
- 'L1521B' on page 1
- 'L1521E' on page 1
- 'L1498' on page 1
- 'G2' on page 1
- 'L1506' on page 2
- 'L1506C' on page 2
- 'L183' on page 7
- 'B5' on page 10
- 'L1544' on page 11
- 'L1498' on page 11
- 'L1517B' on page 11
- 'L694-2' on page 11
- 'L1197' on page 11